# ELASTICITY QUANTIFICATION USING AN EMPIRICAL RELATIONSHIP BETWEEN SINGLE TRANSDUCER –HARMONIC MOTION IMAGING-DERIVED DISPLACEMENT VERSUS OSCILLATION FREQUENCY

*Md Murad Hossain and Elisa E. Konofagou*

Department of Biomedical Engineering, Columbia University, New York, NY, USA

## ABSTRACT

Mechanical properties of tissues are diagnostically relevant. To interrogate mechanical properties via amplitude-modulated acoustic radiation force (AM-ARF)-induced displacement, single-transducer harmonic motion imaging (ST-HMI) modifies the duration of the discrete excitation pulse (DEP) to generate AM-ARF and interleaves the tracking pulses with DEPs to estimate displacement. This study uses a multi-frequency excitation pulse to generate peak-to-peak displacement (P2PD) at 100 to 1000 in steps of 100 Hz simultaneously and then, generates a slope$^{-1}$ image by fitting a regression line to log (P2PD) versus frequency data. Initial feasibility was demonstrated by imaging 6 and 70 kPa inclusion in an 18 kPa background and a 4T1 breast cancer mouse tumor on Day 11 and 27 post-injection of tumor cells. There was a < 1% difference in slope$^{-1}$ values of 6 kPa inclusion when excitation beam pressure varied from 2.4 to 4.1 MPa. Slope$^{-1}$ values were higher for stiffer materials and indicated that the elasticity of tumors was higher on Day 27 versus 11. These results indicate the feasibility of using slope$^{-1}$ as a quantitative indicator of elastic properties.

***Index Terms—*** Acoustic radiation force, harmonic motion imaging, elasticity, displacement, breast cancer.

## 1. INTRODUCTION

Ultrasound elastography (UE) derived mechanical properties like elasticity have been applied to diagnose diseases in the liver, breast, thyroid, prostate, kidney, muscles, carotid artery, and lymph nodes [1]–[4] due to the variation of mechanical properties with the pathological condition of the tissue. One of the UE approaches uses ARF to induce micron-level motion in the tissue and the induced deformation is estimated using typing B-mode style tracking pulses. ARF-based methods either use displacements "on-axis" to the ARF [5]–[8], or shear wave velocity "off-axis" to the ARF [1], [9] or both [10], [11] to assess the mechanical properties. Both "on-axis" and "off-axis" –based methods have their pros and cons. Shear wave velocity is assessed away (i.e., off-axis) from the ARF location over a 2-4 mm axial-lateral window and provides quantitative mechanical properties like elasticity and viscosity [12]. However, shear wave-based methods have poor spatial resolution and are challenged by tissue heterogeneity and reflected waves from the boundaries [13]. In contrast, "on-axis" displacement-based methods provide better mechanical resolution [14] and are less impacted by tissue heterogeneity as the displacements are assessed under the ARF point spread function (i.e., on-axis). However, displacement-based methods provide relative mechanical properties i.e. mechanical properties of a target region with respect to a reference region [15].

"On-axis" ARF-based methods either use pulsed ARF to induced displacements at the broadband frequency range [5], [6], [8], [16] or oscillatory ARF to induce displacement at a specific frequency [7], [15]. The advantage of using oscillatory ARF is the fact that motion at the input oscillation frequency can be easily filtered from motion artifacts. One of the methods which uses oscillatory excitation is harmonic motion imaging (HMI) [7]. HMI uses a focused ultrasound transducer and an imaging transducer to simultaneously generate and track oscillatory motion at 25-100 Hz, respectively, and a 2-D image is generated by mechanically translating both transducers. The current use of two different transducers with a 3-D positioner renders the HMI system highly complex for diagnostic imaging.

To facilitate HMI data acquisitions while preserving the advantages of the oscillatory excitation, Hossain *et al.* proposed a single transducer –HMI (ST-HMI) to generate and map harmonic motion using an imaging transducer only [15], [17]. In ST-HMI, the oscillatory ARF is generated by modulating the excitation pulse duration and the induced motion is tracked by transmitting the tracking pulses interleaving with DEPs. Note that, changes in the excitation pulse duration change the pulse integrated intensity which in turn generates different ARF magnitudes.

Instead of acquiring specific frequency data separately, the objective of this work is to use a multi-frequency excitation pulse (MFEP) [18] to collect displacement at 100 to 1000 Hz in steps of 100 Hz simultaneously and then, empirically derived the relationship between displacement versus frequency. The empirical relationship is demonstrated by experimenting with two inclusions in a standardized phantom and tumors in a breast cancer mouse model.

## 2. METHOD

### 2.1. Generation of the multi-frequency excitation pulse

The MFEP was composed of a sum of sinusoids with the lowest frequency of $f_L$ and was generated as follows:

$$e\,(t) = \sum_{m=1}^{N_{sinusoid}} m^2 \times cos(2\pi m f_L t + \theta_m) \qquad (1)$$

where, $\theta_m$ is 0 or $\pi$ when $m$ is odd or even, respectively and $N_{sinusoid}$ defines the total number of sinusoids with frequencies

of an integer multiple of $f_L$. Therefore, the maximum frequency in $e(t)$ is $N_{sinusoid} \times f_L$. The duration of the excitation pulse is the product of cycle number ($N_{cycle}$) and fundamental period $T_L = 1/f_L$. The multiplication term, $m^2$ , in (1) is added to account for the higher loss in the higher frequencies. Then, $e(t)$ is normalized to contain minimum and maximum pulse duration of $D_{min}$ and $D_{max}$, respectively. Similar to Hossain *et al.* [15], the above continuous excitation pulse (CEP) is sampled to transmit tracking pulses interleaved with DEP (see Fig. 1). The induced displacement was estimated relative to the reference tracking pulse.

### 2.2. Imaging of phantom and 4T1 breast cancer mouse

ST-HMI with MFEP was used to image 6 and 70 kPa inclusions embedded in an 18 kPa background of a commercially available elastic phantom (model 049A, CIRS, Norfolk, VA, USA). The imaging was performed using a Verasonics research system (Vantage 256, Verasonics Inc., Kirkland, WA, USA) equipped with an L7-4 transducer (Philips Healthcare, Andover, MA, USA). The continuous excitation pulse was sampled to transmit 12 DEP (see Fig. 1) with a center frequency of 4 MHz. The tracking pulse was transmitted in-between DEP with center and pulse repetition frequency (PRF) of 6 MHz and 10 kHz respectively. The 34 focused excited and tracking beams [15] were transmitted in a walking aperture sequence to generate a 2-D image with a lateral field of view of 20 mm. To find the impact of ARF magnitude on the empirical relationship, 6 kPa inclusion was imaged by setting excitation beam voltage at 30 and 45 V in Verasoncis. 30 and 45 V correspond to peak negative pressure of 2.4 and 4.1 MPa in the free field, respectively.

*In vivo* ST-HMI of 4T1 breast cancer mouse [15] was performed by the same Vantage system with an L11-5 transducer (Verasonics Inc., Kirkland, WA, USA). For both phantom and mouse imaging, 4 cycles of multi-frequency oscillation were collected. Tumors were generated by injecting $10^5$ 4T1 breast cancer cells. The center frequency of excitation and tracking pulse was 6 and 9 MHz, respectively with a PRF of 15 kHz. The mouse was anesthetized (1- 2% isoflurane in oxygen) in a supine position on a heating pad with their abdominal hair removed during imaging. The mouse was imaged on Day: 11 and 27 post-injection.

### 2.3. ST-HMI data processing

A custom delay-and-sum beamforming [15] was applied to the acquired channel data to construct beamformed radiofrequency data and 1-D normalized cross-correlation with kernel length of 0.6 mm was applied to estimate displacement relative to the reference tracking pulse which yielded in a 3-D dataset (axial x lateral x time) describing axial displacements over time. The differential displacements at each pixel were computed by subtracting displacements between successive time points to remove the slowly varying motion. Then, the differential displacement profile at each pixel was filtered out using a 4$^{th}$ order infinite impulse response bandpass filter to estimate displacements at each frequency. It is noteworthy to mention that filtering of

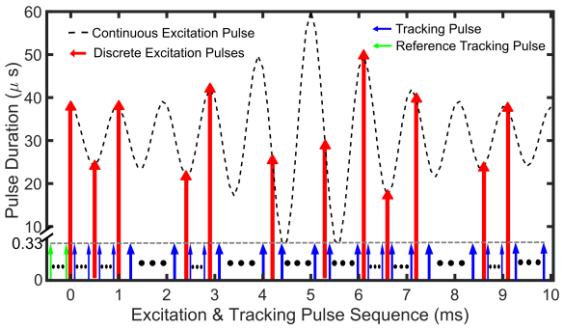


**Fig 1**: 1-cycle of tracking pulses and discrete excitation pulses for multi-frequency ST-HMI. Discrete excitation pulses are generated by sampling continuous excitation pulse with $f_L$ = 100 Hz, $N_{sinusoid}$ = *10*, *Dmin* = 5 µs, and *Dmax* = 60 µs. Displacements were calculated with respect to the reference tracking pulse.

differential displacement profiles was performed separately at each frequency. Then, the P2PD image at each frequency was generated by calculating P2P over cycles.

We empirically found that the log (P2PD) is linearly related to the oscillation frequency. Therefore, a 2-D image of the slope was generated by fitting a line at each pixel. As the generated slope was inversely related to stiffness, an inverse of the slope (slope$^{-1}$) was calculated to have higher values for the stiffer materials.

## 3. RESULTS AND DISCUSSION

Fig. 1 shows the 1-cycle of CEP with $f_L$ = 100 Hz, $N_{sinusoid}$ = *10*, *Dmin* = 5 µs, and *Dmax* = 60 µs for the multi-frequency ST-HMI. According to equation (1), CEP contained frequencies from 100 Hz to 1000 Hz in steps of 100 Hz. The CEP was sampled to transmit 12 DEPs with interleaved tracking pulses. Note, the duration of the DEP changes but all tracking pulses duration is 0.33 µs. Acoustic intensity is different for pulses with a different duration which in turn generates different magnitude ARF. While Fig. 1 is shown for 1-cycle, 4-cycles of MFEP were used to collect data.

Fig. 2 (a) shows the exponential relationship between P2PD versus oscillation frequency at 2.4 and 4.1 MPa pressure on a background pixel of the phantom. Note, all P2PDs were generated simultaneously by using the above MFEP. The higher pressure generated higher P2PD due to the higher ARF magnitude. The P2PD at each frequency was normalized by the P2PD at 100 Hz and panel (b) shows that the relationship between log (normalized P2PD) versus frequency is linear for both background and inclusion pixel. While the intercept of the fit varied between 2.4 versus 4.1 MPa, the slope$^{-1}$ in background and inclusion was similar for both pressures. This result indicates that slope$^{-1}$ does not depend on the ARF magnitude which is generally unknown in the tissue because ARF magnitude depends on the acoustic attenuation and sound speed. Fig. 3 shows fit performance in the 70 kPa inclusion and mouse tumor. The $R^2$ of the fit was 0.97-0.99 in the background or healthy tissue whereas the $R^2$ was 0.94, 0.84, and 0.91 in the 70 kPa inclusion and tumor on

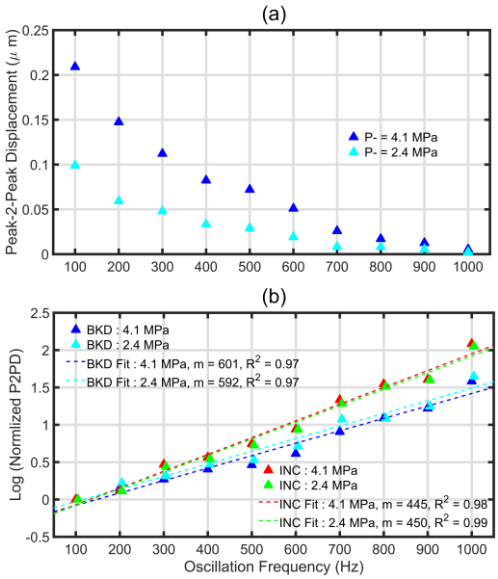


**Fig 2**: (a) Peak to peak displacement (P2PD) versus oscillation frequency of a background (BKD) pixel (b) log (normalized P2PD) versus frequency of BKD and 6 kPa inclusion (INC) pixels with slope$^{-1}$ (m) and $R^2$ of the fit for the excitation beam pressure of 2.4 and 4.1 MPa. The pixel location is on Fig. 4.

Day 11 and 27, respectively. Despite reduction in $R^2$, the slope$^{-1}$ was higher in both inclusions and tumor compared to the background and healthy tissue. The slope$^{-1}$ was calculated for each pixel to generate a 2-D image.

Fig. 4 shows B-mode and slope$^{-1}$ images of 6 and 70 kPa inclusion embedded in an 18 kPa background. Four observations are notable. First, slope$^{-1}$ was lower or higher with respect to the background for softer or stiffer inclusion, respectively. Second, slope$^{-1}$ images of 6 kPa inclusion are fairly similar for 4.1 and 2.4 MPa. There was a slight difference between 4.1 versus 2.4 MPa around and above 25 mm axial location in the background (panels b and c). This may be due to a lower ARF magnitude above 25 mm axial. As the ARF diverges from the focus (35 mm), the magnitude decreases. Third, 70 kPa inclusion does not appear as homogeneous as 6 kPa inclusion. Note, the $R^2$ of the fit was lower in the 70 versus 6 kPa inclusion (Figs. 2b and 3a ). It may be due to the particular characteristics of 70 kPa inclusions or slope$^{-1}$ may be impacted differently for softer versus stiffer inclusions. Future studies will investigate this aspect by imaging different stiffer inclusions. Finally, the background below the inclusion has a different amplitude than the background at the same axial depth but left or right of inclusion. This may be due to boundary effects. In the future, FEM simulation [6] will be performed to investigate why this effect is prominent below the inclusion boundaries. Note, the goal of the slope$^{-1}$ calculation is not to improve the detectability of inclusions rather quantify elasticity. The P2PD can be used to better delineate inclusion.

Fig. 5 shows *in vivo* B-mode and slope$^{-1}$ images of a mouse tumor on Day 11 and 27 post-injection of the tumor cells. Two observations are notable. First, the tumor grew in size over time. Second, higher slope$^{-1}$ indicates that the tumor became stiffer with growing size with the ingression of tumor cells. In the future, we will investigate the impact of the size of inclusion/tumor on slope$^{-1}$. Table 1 summarizes the median ± std of slope$^{-1}$ values in the ROI of the phantom and tumor.

## 4. CONCLUSION

This study demonstrates that the slope$^{-1}$ of a linear relationship between MFEP-derived log (normalized P2PD)

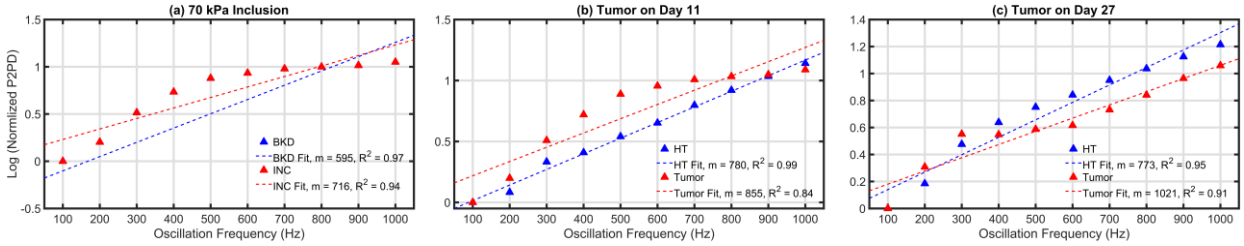


**Fig 3**: Log (normalized peak-to-peak displacement, P2PD) versus frequency of a pixel on the (a) background (BKD) and inclusion (INC) of 70 kPa inclusion and healthy tissue (HT) and tumor on Day (b)11 and (c) 27 post-injection of tumor cells with slope$^{-1}$ (m) and $R^2$ of the fit. The pixel location is shown on Figs. 4 and 5.

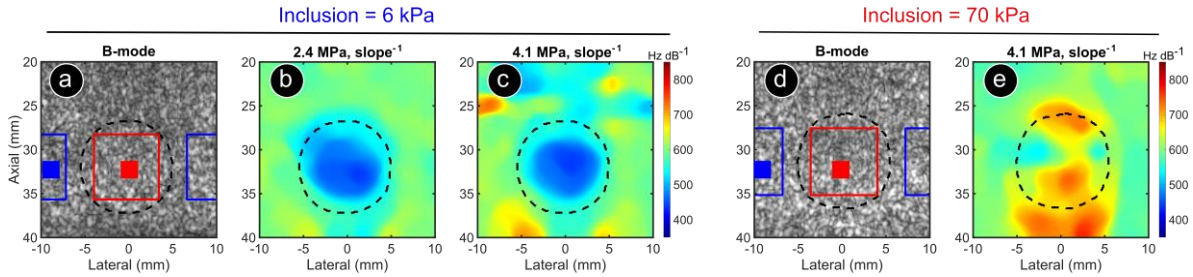


**Fig 4**: (a,d) B-mode and (b,c,e) slope$^{-1}$ images of 6 and 70 kPa inclusion embedded in a 18 kPa background. Black, red, and blue contours represent inclusion boundary and ROI in inclusion and backgrond, respectively. Blue and red filled rectangle represent pixel location used to represent fit and slope in Figs. 2 and 3.

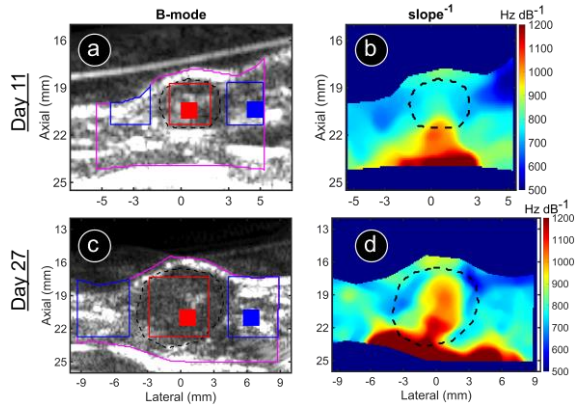


**Fig. 5**: (a,c) *In vivo* B-mode and (b,d) slope$^{-1}$ images of a mouse tumro on Day 11 and 27 post-injection of the tumor cells. Black, red, blue, and magenta contours represent inclusion boundary, ROI in tumor and healthy tissue, and slope$^{-1}$ image field of view respectively. Blue and red filled rectangle represent pixel location used to represent fit in the Fig. 3.

**Table 1**: Median ± standard deviaton (std) of slope$^{-1}$ values in the region of interest (ROI) of inclusion/tumor (Num) and backgound/healthy tissue (Denum) of phantom/mouse.

| Materials Type | Region Name | Median ± std | Ratio = Num / Denum |
|---|---|---|---|
| 6 kPa, 4.1 MPa | Inclusion<br>Background | 475.7 ± 21.8<br>600.5 ± 24.5 | 0.8 |
| 6 kPa, 2.4 MPa | Inclusion<br>Background | 478.7 ± 21.9<br>603.2 ± 24.6 | 0.8 |
| 70 kPa, 4.1 MPa | Inclusion<br>Background | 655.1 ± 25.6<br>587.3 ± 24.2 | 1.12 |
| Tumor, Day 11 | Tumor<br>Healthy tis. | 773.6 ± 27.8<br>699.2 ± 26.4 | 1.11 |
| Tumor, Day 27 | Tumor<br>Healthy tis. | 940.2 ± 30.7<br>777.5 ± 27.9 | 1.21 |

versus oscillation frequency quantifies the mechanical properties of the materials and does not depend on the ARF magnitude. The slope$^{-1}$ was higher for stiffer inclusion and differentiated the tumor stiffness at two different time-points during progression *in vivo*. Future work will investigate the relationship between slope$^{-1}$ versus viscoelasticity of tissues and compare slope$^{-1}$ images with shear-wave-based methods.

## 5. ACKNOWLEDGMENTS

This work was supported by the NIH under Grant R01 CA228275. The authors thank Drs. Saurabh Singh, Indranil Basu, and Chandan Guha from the Albert Einstein College of Medicine and Montefiore Medical Center, Bronx, NY, USA, for providing the cancer cell for the mouse study.

## 6. COMPLIANCE WITH ETHICAL STANDARDS

Cancer induction and imaging protocols for mouse were reviewed and approved by the Columbia University Irving Medical Institutional Animal Care and Use Committee.

## 7. REFERENCES

[1] R. M. S. Sigrist, J. Liau, A. El Kaffas, M. C. Chammas, and J. K. Willmann, "Ultrasound Elastography: Review of Techniques and Clinical Applications," *Theranostics*, vol. 7, no. 5, pp. 1303–1329, 2017.

[2] M. M. Hossain *et al.*, "Evaluating Renal Transplant Status Using Viscoelastic Response (VisR) Ultrasound.," *Ultrasound Med. Biol.*, vol. 44, no. 8, pp. 1573–1584, May 2018.

[3] M. M. Hossain *et al.*, "Mechanical Anisotropy Assessment in Kidney Cortex Using ARFI Peak Displacement: Preclinical Validation and Pilot In Vivo Clinical Results in Kidney Allografts.," *IEEE Trans. Ultrason. Ferroelectr. Freq. Control*, vol. 66, no. 3, pp. 551–562, Mar. 2019.

[4] M. M. Hossain and C. M. Gallippi, "Quantitative Estimation of Mechanical Anisotropy using Acoustic Radiation Force (ARF)-Induced Peak Displacements (PD): In Silico and Experimental Demonstration.," *IEEE Trans. Med. Imaging*, vol. PP, no. X, pp. 1–14, Jan. 2022.

[5] K. Nightingale, M. S. Soo, R. Nightingale, and G. Trahey, "Acoustic radiation force impulse imaging: in vivo demonstration of clinical feasibility.," *Ultrasound Med. Biol.*, vol. 28, no. 2, pp. 227–35, Feb. 2002.

[6] M. M. Hossain and C. M. Gallippi, "Viscoelastic Response Ultrasound Derived Relative Elasticity and Relative Viscosity Reflect True Elasticity and Viscosity: In Silico and Experimental Demonstration.," *IEEE Trans. Ultrason. Ferroelectr. Freq. Control*, vol. 67, no. 6, pp. 1102–1117, 2020.

[7] E. E. Konofagou and K. Hynynen, "Localized harmonic motion imaging: Theory, simulations and experiments," *Ultrasound Med. Biol.*, vol. 29, no. 10, pp. 1405–1413, 2003.

[8] M. R. Selzo, C. J. Moore, M. M. Hossain, M. L. Palmeri, and C. M. Gallippi, "On the Quantitative Potential of Viscoelastic Response (VisR) Ultrasound Using the One-Dimensional Mass-Spring-Damper Model.," *IEEE Trans. Ultrason. Ferroelectr. Freq. Control*, vol. 63, no. 9, pp. 1276–87, 2016.

[9] A. P. Sarvazyan, O. V. Rudenko, S. D. Swanson, J. B. Fowlkes, and S. Y. Emelianov, "Shear wave elasticity imaging: a new ultrasonic technology of medical diagnostics.," *Ultrasound Med. Biol.*, vol. 24, no. 9, pp. 1419–35, Nov. 1998.

[10] J. Vappou, C. Maleke, and E. E. Konofagou, "Quantitative viscoelastic parameters measured by harmonic motion imaging," *Phys. Med. Biol.*, vol. 54, no. 11, pp. 3579–3594, Jun. 2009.

[11] C. Amador Carrascal, S. Chen, M. W. Urban, and J. F. Greenleaf, "Acoustic Radiation Force-Induced Creep–Recovery (ARFICR): A Noninvasive Method to Characterize Tissue Viscoelasticity," *IEEE Trans. Ultrason. Ferroelectr. Freq. Control*, vol. 65, no. 1, pp. 3–13, Jan. 2018.

[12] P. Kijanka and M. W. Urban, "Local Phase Velocity Based Imaging (LPVI) of Viscoelastic Phantoms and Tissues," *IEEE Trans. Ultrason. Ferroelectr. Freq. Control*, vol. 3010, no. c, pp. 1–1, 2020.

[13] Y. S. Cho, S. Lim, Y. Kim, T. Y. Kim, W. K. Jeong, and J. H. Sohn, "Abdominal Wall Thickness Affects Liver Stiffness Measurements by 2-D Shear Wave Elastography in Patients with Chronic Liver Disease," *Ultrasound Med. Biol.*, vol. 00, no. 00, pp. 1–7, Jul. 2019.

[14] P. J. Hollender, S. J. Rosenzweig, K. R. Nightingale, and G. E. Trahey, "Single- and Multiple-Track-Location Shear Wave and Acoustic Radiation Force Impulse Imaging: Matched Comparison of Contrast, Contrast-to-Noise Ratio and Resolution," *Ultrasound Med. Biol.*, vol. 41, no. 4, pp. 1043–1057, 2015.

[15] M. M. Hossain, N. Saharkhiz, and E. E. Konofagou, "Feasibility of Harmonic Motion Imaging Using a Single Transducer: In Vivo Imaging of Breast Cancer in a Mouse Model and Human Subjects," *IEEE Trans. Med. Imaging*, vol. 40, no. 5, pp. 1390–1404, May 2021.

[16] M. W. Urban, A. Alizad, W. Aquino, J. F. Greenleaf, and M. Fatemi, "A Review of Vibro-acoustography and its Applications in Medicine.," *Curr. Med. Imaging Rev.*, vol. 7, no. 4, pp. 350–359, Nov. 2011.

[17] M. M. Hossain, N. Saharkhiz, and E. E. Konofagou, "In Vivo Demonstration of Single Transducer Harmonic Motion Imaging (ST-HMI) in a Breast Cancer Mouse Model and Breast Cancer Patients," in *2020 IEEE International Ultrasonics Symposium (IUS)*, 2020, vol. 2020-Septe, pp. 1–4.

[18] M. M. Hossain and E. Konofagou, "Feasibility of a single-transducer harmonic motion imaging using frequency-based simultaneous multiple harmonic oscillation excitation pulses," *J. Acoust. Soc. Am.*, vol. 148, no. 4, pp. 2600–2600, Oct. 2020.